

Article

Mechanism and Experimental Study on Electrostatic Atomization Using Needle-Shaped Electrodes

Hao Ma and Min Yang *

School of Mechanical and Automotive Engineering, Qingdao University of Technology, Qingdao 266520, China; ytdxhaoma@163.com

* Correspondence: 18266487809@163.com

Abstract: The conventional pneumatic Minimum Quantity Lubrication (MQL), when not properly designed, may have poor atomization and insufficient wetting performance, resulting in higher oil mist concentration and poor film formation ability in the cutting zone. The intervention of an external electric field can change the atomization mechanism of microdroplets and enhance the lubrication and cooling capability of MQL. However, the mechanism of the effect of jet parameters on the atomization performance of Electrostatic Minimum Quantity Lubrication (EMQL) under the synergistic effect of multiple fields has not been fully analyzed. In this paper, based on the designed needle electrode charging nozzle, the atomization medium charging and atomization mechanisms are investigated, and a mathematical model of the volume average diameter of droplets (VAD) is established. Based on multi-parameter atomization experiments, the electrode conical jet atomization model is validated and the mechanism of the influence of jet parameters on the atomization characteristics is analyzed. The results show that the VAD is negatively correlated with air pressure and electrical. The atomization performance of the droplets was improved under the applied voltage condition, which was manifested by the obvious refinement of the VAD, with a maximum reduction of 34.67%, a maximum reduction of 20% in the droplet group size distribution span (R.S.), and a different degree of reduction in the percentage concentration of fine particulate matter. In addition, the model fitted well with the experimental values, with an overall error of about 10%.

Keywords: electrostatic atomization; minimum quantity lubrication; needle electrode; cone jet; multifield energy coupling



Citation: Ma, H.; Yang, M.

Mechanism and Experimental Study on Electrostatic Atomization Using Needle-Shaped Electrodes. *Lubricants* **2023**, *11*, 235. <https://doi.org/10.3390/lubricants11060235>

Received: 6 May 2023

Revised: 19 May 2023

Accepted: 24 May 2023

Published: 26 May 2023



Copyright: © 2023 by the authors. Licensee MDPI, Basel, Switzerland. This article is an open access article distributed under the terms and conditions of the Creative Commons Attribution (CC BY) license (<https://creativecommons.org/licenses/by/4.0/>).

1. Introduction

Minimum Quantity Lubrication (MQL) is a clean, efficient, and low-consumption new method for supplying cooling lubricants, which avoids the high cost of using mineral-based cutting fluids in traditional flooding lubrication and poses a threat to the natural environment and operator health. MQL has shown excellent cooling and lubrication performance in different types of cutting experiments conducted by many scholars [1–4]. It has been widely used in the field of mechanical component processing and manufacturing [5]. Although MQL has achieved a reduced supply of lubricants, there are still the following technical bottlenecks: trace lubricants rely on high-pressure gas atomization, and their droplet size, distribution, and transportation are difficult to accurately control with the disturbance of the gas flow field, often accompanied by the generation of inhalable fine particulate matter less than 10 microns in diameter or less than 2.5 microns in diameter (PM₁₀, PM_{2.5}) [6–8], which still pose a certain threat to the environment and human health; At the same time, the high concentration of oil mist in the micro lubrication cutting area of pneumatic atomization results in poor film forming ability, leading to insufficient wetting performance. How to refine the volume average diameter of droplets (VAD) and improve the uniformity of droplet group size distribution span (R.S.) is a bottleneck problem that restricts the development of MQL [9,10].

Based on the urgent needs and technical bottlenecks mentioned above, researchers have proposed the Electrostatic Minimum Quantity Lubrication (EMQL), in which a high-voltage electric field is used to control the jet, and a high-voltage electrostatic field is generated between the nozzle energized and the workpiece, and the oil mist ejected from the nozzle is charged in a contact charge or corona charge manner, and under the action of the electrostatic field, the oil mist is efficiently and uniformly ejected into the cutting area of the workpiece along the direction of the electric field lines [11,12]. EMQL uses electrostatic and airflow fields to synergistically atomize, effectively reducing the VAD and the R.S., and improving their deposition and permeability performance [13–15]. Researchers have conducted theoretical and experimental research on the mechanism of electrostatic atomization cutting and grinding. Reddy and Yang et al. [16] applied an electrostatic lubrication system for the first time in the drilling process of SCM 440 steel. The unique atomization of this technology was found to be effective not only in reducing the concentration of oil mist in the air but also in improving the performance of the cutting lubricant. The results of an experimental study conducted by Xu et al. [17] for milling AISI 304 stainless steel showed that the cutting forces obtained by EMQL were lower at different cutting rates, and the difference became more pronounced as the cutting rate increased. The efficient utilization of cutting fluid relies on its ability to wet the tool-chip and tool-workpiece interface in the shortest possible time, while under interrupted milling conditions, increasing the cutting rate will lead to increased pressure in the cutting area, smaller contact gap between the tool-workpiece, and is not conducive to fluid wetting, while charged fluid wetting is more favorable. Huang and several other scholars [18–21] conducted experiments on nickel-based alloys, 45 steel, Titanium alloy, and other materials, the results of multi-type EMQL cutting experiments showed that compared to the MQL machining method, EMQL is effective in reducing cutting forces and cutting temperatures, improving workpiece surface quality, and extending tool life. Jia et al. [22–24] in an experiment of MQL grinding of Ti-6Al-4V titanium alloy with soybean oil as the base lubricant, concluded that the friction force and grinding temperature were significantly higher than those of the cast type, while the friction force was only about 86% and the grinding temperature was 36.9% lower when grinding with EMQL, and it was significantly smaller than that of the conventional cast method, which indicated that the charged droplets with good penetration influence the friction in the cutting area, which also greatly improves the heat transfer performance of the lubricant.

In addition, mechanism research of EMQL processing has been carried out along with studies of the atomization characteristics of EMQL nozzles and the mechanism of electrostatic field action. Initially, Taylor, while studying the deformation of droplets under an electric field, found that droplets would form a Taylor cone structure and generate a jet and then fracture, which has since attracted the attention of a large number of researchers [25]. Li et al. [26] conducted a systematic study on the formation and destruction modes of Taylor cones under electrostatic spray conditions using a cavity atomization device and conducted an in-depth theoretical and experimental study on the cone angle, long-short axis relationship, cone shape, and destruction period of Taylor cones. It was found that electric field strength, liquid viscosity, and surface tension play a significant role in the formation and breakup of Taylor cones. Nie et al. [27] constructed a nano-scale Taylor cone model using a multi-body dissipative particle dynamics approach. The sharpening process and the breaking process of Taylor cones under different electric field strengths and different charge concentrations were systematically investigated. Under the strong electric field, the hemispherical droplet becomes sharp with time and evolves into a conical shape. Then a fine jet is emitted from the conical tip. Finally, after jet fragmentation, the cone shrinks into a hemisphere. These deformation processes occur several times until no charge is emitted from the cone tip. It was found that the electric field force is responsible for the jet emission, while the Coulomb force causes the jet to break up. As the electric field strength increases, the breakup time also increases. However, the breakup time decreases

with increasing charge concentration. This suggests that conducting liquids with low conductivity and subject to strong electric fields are more prone to pulsation rupture.

Compared with the MQL technology, the atomization mechanism will change after the intervention of an electric field, and there is little research on the atomization mechanism under multi-field synergy, and there is a lack of evaluation of EMQL technology in terms of safety, stability, and applicability, which is obviously unfavorable to the development of EMQL technology. Based on this, this paper designs a needle electrode electrostatic atomization two-way flow nozzle to explore the atomization mechanism of needle electrode cone jet, establishes the atomization model of the nozzle, validates the model, and analyzes the atomization characteristics through atomization experiments, and provides a basis and technical reference for the application of EMQL technology in cutting processing.

2. Nozzle Structure

For low-conductivity lubricants used in MQL, such as vegetable oils and synthetic greases, contact charging exhibits higher charging efficiency. Additionally, the contact charging spray assembly structure is simpler in terms of design. Existing two-phase flow atomization nozzles typically have a metallic outer shell and outlet at the end, which can be directly connected to the electrostatic device via a conductor to function as a contact charging nozzle. However, such nozzles lack a dedicated electrostatic interface, and directly connecting the conductor to the metallic outer shell exposes the electrode to the air, posing safety hazards to machine tools and operators. To address this issue, the nozzle is modified and upgraded by changing the electrode to a needle-shaped structure located at the nozzle's center and replacing the nozzle casing and gas-liquid passages with insulating materials. The structure and physical representation of the nozzle is shown in Figure 1. An electrostatic interface is reserved at the top of the nozzle, and the high-voltage cable's internal wire core end is polished flat to make contact with the similarly polished flat end of the electrode needle, forming a contact connection when pressed together. Once the nozzle is connected to the electrostatic device, the lubricant enters the liquid pipe through the inlet, contacts the electrode needle for charging, and subsequently atomizes within the atomization chamber.

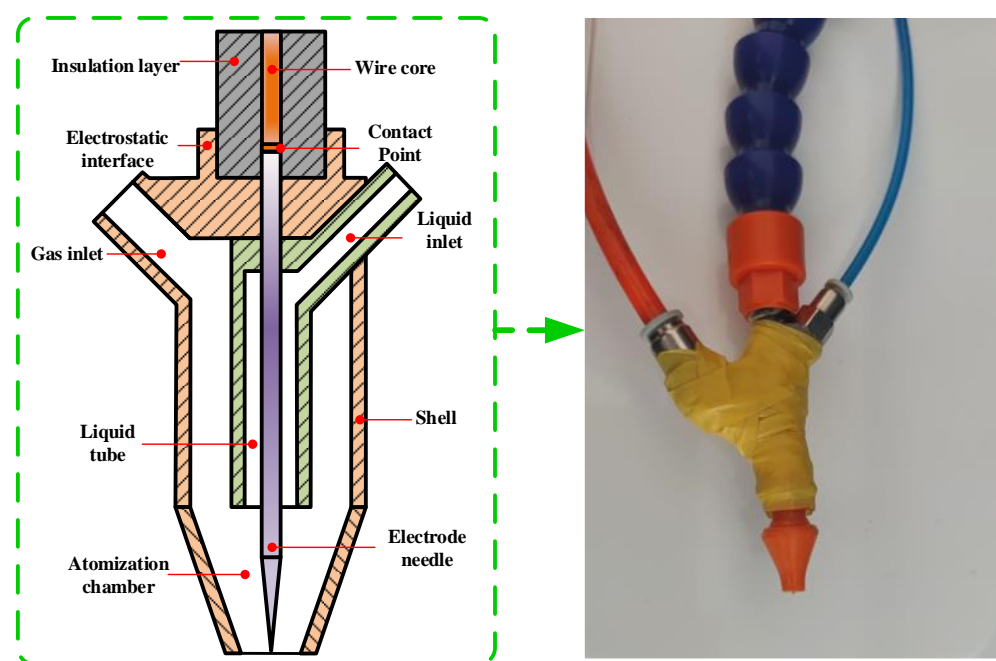


Figure 1. Needle electrode electrostatic nozzle.

3. Atomization Mechanism

3.1. Lubricant Charging Characteristics

Contact charging, corona charging, and induction charging may coexist between the needle-plate electrodes. Since induction charging typically uses a ring-shaped electrode and has a small charge amount, its influence can be approximately ignored during the charging process. The primary consideration is given to contact charging and corona charging.

When the needle electrode contacts the jet, contact charging is the primary mechanism at work. The needle-plate electrode pair can be approximated as a capacitor, and according to the capacitance calculation formula, the charge quantity q_1 (C) by the jet can be represented as:

$$q_1 = \frac{\varepsilon_r \varepsilon_0 S_n}{L} U \quad (1)$$

where S_n is the facing area of the two poles (m^2); ε_r is the relative permittivity of air; ε_0 is the vacuum permittivity ($8.85 \times 10^{-12} \text{ C/V}\cdot\text{m}$); U is the nozzle voltage (V); L is the distance between the poles (m).

When the needle electrode is not in contact with the jet, the droplets generated under the action of gas drag forces move downstream of the nozzle and enter the corona zone for corona charging. Droplets in the discharge area near the electrode collide with and adhere to ions, thus undergoing charging. After being charged, the droplets themselves generate an electric field, which strengthens as the charge amount increases. Charging ends when the droplet's electric field balances the external electric field. During this process, droplets subjected to external forces continuously break into smaller droplets. Before breaking, the charge amount q_2 (C) of the droplets under corona action is [28]:

$$q_2 = \frac{3k_1 \pi \varepsilon_0 \varepsilon_r E D^2}{\varepsilon_r + 2} \frac{t}{t + t_0} \quad (2)$$

where D is the droplet diameter (m); E is the electric field strength (V/m); k_1 is a correction factor (dimensionless); t is the charging time (s); t_0 is the time constant, with a standard value of $2 \times 10^{-3} \text{ s}$. According to the Mason theoretical model, an electric field strength model can be constructed at a distance x (m) from the tip of the electrode as follows [22]:

$$E_x = \frac{2U}{(r + 2x) \ln[(r + 2L)/r]} \quad (3)$$

where r is the discharge electrode radius (m). When x takes the value of 0, the electric field strength at the tip of the needle can be obtained as follows:

$$E_{x=0} = \frac{2U}{r \ln[(r + 2L)/r]} \quad (4)$$

The prerequisite for corona charging is that the voltage applied to the electrode reaches the discharge threshold and generates a corona. According to past empirical formulas, the threshold field strength E_s (V/m) for corona generation is:

$$E_s = E_0 \left(1 + \frac{K}{(r/2)^{1/2}} \right) \quad (5)$$

where E_0 is the uniform electric field strength for a breakdown of a 1 cm gap under standard pressure (3100 kV/m); K is a correction factor ($3.08 \times 10^{-2} \text{ m}^{1/2}$). The calculation result of Formula (5) can be substituted into Formula (3) to infer the corresponding threshold voltage.

During the corona charging process, ions in the discharge area are mainly produced by ionizing air, which is mainly composed of nitrogen and oxygen. Rare gases with extremely low contents can be ignored. Under an electric field, nitrogen and oxygen molecules

either lose electrons to become ions or undergo adsorption, compound, and other chemical reactions by colliding with electrons and ions. The main particle chemical reactions that occur are shown in Table 1:

Table 1. Chemical reactions of main particles.

No.	Chemical Reaction	Reaction Type	Reaction Rate Constant
1	$e + O_2 \rightarrow 2e + O_2^+$	Collisional Ionization	$f(\epsilon)$ [29]
2	$e + O_2 \rightarrow O_2^-$	Adsorption Reaction	$f(\epsilon)$
3	$e + 2O_2 \rightarrow O_2^- + O_2$	Adsorption Reaction	2.0×10^{-41} (300/Te)
4	$e + O_2^+ \rightarrow O_2$	Compound Reaction	5×10^{-14}
5	$O_2^- + O_2^+ \rightarrow 2O_2$	Compound Reaction	5×10^{-12}
6	$e + N_2 \rightarrow 2e + N_2^+$	Collisional Ionization	$f(\epsilon)$
7	$e + N_2 \rightarrow N_2^-$	Adsorption Reaction	$f(\epsilon)$
8	$e + 2N_2 \rightarrow N_2 + N_2^-$	Adsorption Reaction	2.0×10^{-41} (300/Te)
9	$e + N_2^+ \rightarrow N_2$	Compound Reaction	5×10^{-14}
10	$N_2^- + N_2^+ \rightarrow 2N_2$	Compound Reaction	5×10^{-14}

Where Te is the Electron temperature (K). Charged droplets mainly have charges distributed on their surfaces. Subject to Coulomb forces and electric field forces, the surface tension of the droplets is reduced. According to the principle of energy conservation and virtual work, the effective surface tension σ^* (N/m) of charged droplets is [30]:

$$\sigma^* = \sigma - \frac{Q_Z^2}{64\pi^2 \epsilon_0 \epsilon_r R^3} \quad (6)$$

where σ is the liquid surface tension (N/m); Q_Z is the total charge of the droplet (C); R is the droplet radius (m).

The expression of the charge amount and effective surface tension shows that the factors affecting their changes, in addition to external factors, are also related to the relative permittivity of the lubricant itself. In actual use, to better improve the charging performance and reduce the effective surface tension, a certain proportion of nanoparticles with higher relative permittivity is added to the lubricant to improve the atomization effect.

The relative permittivity, an important indicator reflecting the electrical characteristics of dielectric and insulating materials, is used to reflect the relative capacity of materials to store electrostatic energy in an electric field. The relative permittivities of several types of common nanoparticles are shown in Table 2. Under ideal conditions (such as low temperature), Carbon nanotubes (CNTs) can have a relative permittivity of up to 205.5.

Table 2. Parameters of nanoparticles [31,32].

Nanoparticles	Density (g/cm ³)	Relative Dielectric Constant
SiO ₂	2.2	3.9
Fe ₂ O ₃	5.27	14.2
Al ₂ O ₃	3.7	4.9
CNTs	1.3	205.5

After the lubricant and nanoparticles are mixed without undergoing a chemical reaction, their respective physical properties remain unchanged. The increase in the dielectric constant of the mixture compared to the pure lubricant depends on the addition ratio of nanoparticles. The complex dielectric constant ϵ^* of the mixture can be expressed as [33]:

$$\epsilon^* = \frac{V_l}{V} \epsilon_l + \frac{V_s}{V} \epsilon_s \quad (7)$$

where V is the mixture volume (m³); V_l is the liquid volume (m³); V_s is the nanoparticle volume (m³); ϵ_l is the liquid relative permittivity; ϵ_s is the nanoparticle relative permittivity.

The above formula can be converted into an expression related to the nanoparticle mass m_s (kg):

$$\varepsilon^* = \frac{V_l}{V} \varepsilon_l + \frac{m_s}{V \cdot \rho_s} \varepsilon_s \quad (8)$$

where ρ_s is the nanoparticle density (kg/m^3).

3.2. Cone-Jet Model

The essence of liquid atomization is the forced detachment of surface elements by external forces and the subsequent contraction and agglomeration of these elements under the influence of surface tension to form droplets, as shown in Figure 2. The initial jet produced by the nozzle typically consists of a liquid column, a liquid film, or larger liquid clusters. The external forces acting on the liquid mainly include gravity and gas drag, while the internal forces consist of surface tension and viscous forces. For liquids with high fluidity, the influence of viscous forces can be neglected. When the external forces exceed the internal forces, droplet detachment occurs. Similarly, when a droplet reaches this condition, it can further break up into smaller droplets.

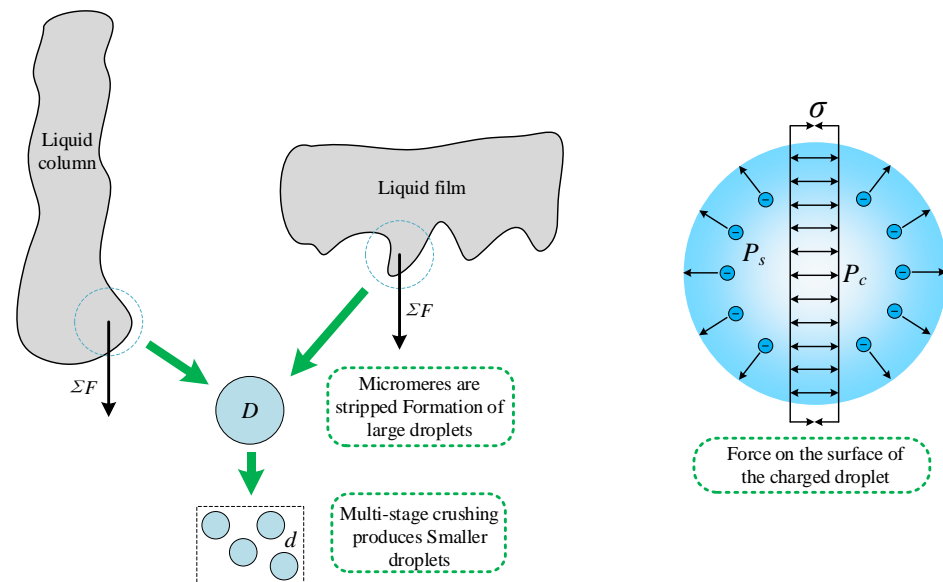


Figure 2. Droplet force process.

Upon the addition of an electric field, the jet becomes charged. Taking a spherical droplet as an example, the repulsion between a large number of similar charges on its surface due to the Coulomb force reduce the droplet's surface tension, undoubtedly exacerbating the breakup process of the liquid column/liquid film/liquid cluster.

The needle-shaped electrode in the nozzle designed in this study is located within the liquid tube, and a gap is formed between the surface of the electrode base and the inner wall of the liquid tube. The lubricant flows out of the gap and forms a liquid film on the surface of the electrode needle. Due to the drainage effect of the electrode needle, the liquid converges at the tip of the needle electrode, where the thickness of the liquid film is the greatest. As a result of the influence of the airflow field and electric field, disturbances in the liquid film are most likely to occur at this location, as shown in Figure 3.

When the electrode needle is energized, the charges at its tip accumulate and contact-charge the liquid film. As the liquid film experiences disturbances, the uniformity of the surface charge also changes, leading to an increase in local forces. The liquid undergoes stretching and deformation, forming a conical body. The charge density is higher near the base of the cone due to the electric field, and when the external force is large enough, the tip of the cone is stretched and detaches from the cone, producing a jet. The number of

conical bodies increases with increasing voltage, and under a constant liquid supply, the more conical bodies there are, the smaller the diameter of the jets they produce [34].

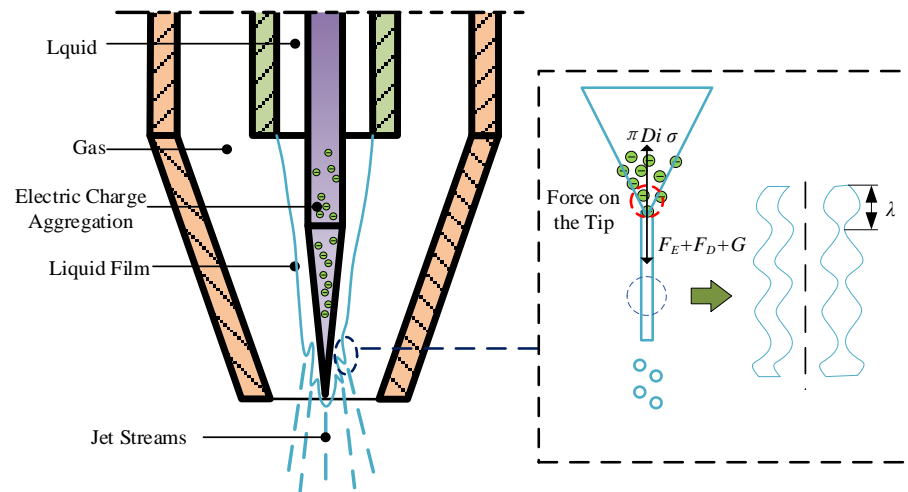


Figure 3. Atomization process.

Upon the formation of a jet at the base of the cone, a shear force arises at the gas-liquid interface due to the difference in gas and liquid velocities, causing symmetric or asymmetric waves on the liquid surface, with symmetric waves being more common [35,36]. When the amplitude of the jet wave reaches a certain level, it breaks up, and each broken liquid unit contracts under the influence of surface tension to form a spherical droplet. According to the principle of equal volume, we obtain

$$D = \sqrt[3]{\frac{3D_i^2\lambda}{2}} \quad (9)$$

where D is the droplet diameter (m); D_i is the jet diameter (m); λ is the wavelength (m).

In addition to the electric field force (F_E), the unit at the base of the cone is also subjected to external forces such as gas drag (F_D) and gravity (G). The external forces overcome the adhesion force to generate a cone jet, where the adhesion force is equivalent to surface tension. Based on the balance of internal and external forces, we deduce

$$\pi D_i \sigma^* = F_D + F_E + G \quad (10)$$

When droplets move through air or other viscous fluids, pressure resistance and friction resistance are generated. The combined effect of these two forces results in gas drag (F_D), which can be expressed as follows:

$$F_D = \frac{1}{8} C_D (\pi D_i^2) \rho_g v_g^2 \quad (11)$$

where C_D represents the drag coefficient; ρ_g represents air density (kg/m^3); v_g represents the gas flow velocity (m/s). The drag coefficient is a function of the Reynolds number, and the expression is as follows [37]:

$$C_D = \begin{cases} \frac{24}{\text{Re}} & \text{Re} < 1 \\ \frac{24}{\text{Re}} \left(1 + \frac{3}{16} \text{Re}\right) & \text{Re} > 1 \end{cases} \quad (12)$$

In a nonuniform electric field, the electric field force acting on the charged droplets varies with the electric field strength and the amount of charge:

$$F_E = Q_Z E \quad (13)$$

where Q_Z is the total charge of the droplet (C); E is the electric field strength at the droplet's location (V/m). Considering the gas drag, electric field force, and gravity, we can determine the jet diameter as

$$D_i = \frac{8\sigma^*L}{C_D\rho_g v_g^2 L + 2\varepsilon_r \varepsilon_0 UE + 2\rho_l h_l gL} \quad (14)$$

When considering the gas-liquid interface as a discontinuous velocity interface where the thickness of the vortex approaches zero, based on the Kelvin-Helmholtz (K-H) wave instability theory, and under the condition where the liquid phase density is much larger than the gas phase density ($\rho_l \gg \rho_g$), we can establish the dispersion equation for the gas-liquid disturbance interface as follows [35,36]:

$$\omega = k \frac{\rho_l v_l + \rho_g v_g}{\rho_l + \rho_g} \pm i \frac{k}{\rho_l + \rho_g} \sqrt{\rho_l \rho_g (v_g - v_l) - (\rho_l + \rho_g) \sigma^* k} \quad (15)$$

where ω is the surface wave growth rate; k is the surface wave wavenumber. The maximum growth rate, ω_{max} , is

$$\omega_{max} = (2/3\sqrt{3}) (\rho_g/\rho_l)^{1/2} (\rho_g v_g^3/\sigma^*) \quad (16)$$

At the maximum growth rate, the corresponding wavenumber is

$$k = \frac{2\rho_g v_g^2}{3\sigma^*} \quad (17)$$

Based on the relationship between wavelength and wavenumber, λ is

$$\lambda = \frac{2\pi}{k} = \frac{3\pi\sigma^*}{\rho_g v_g^2} \quad (18)$$

In summary, the VAD after the cone jet breakup is

$$D = \sqrt[3]{\left(\frac{8\sigma^*L}{C_D\rho_g v_g^2 L + 2\varepsilon_r \varepsilon_0 UE + 2\rho_l h_l gL}\right)^2 \frac{9\pi\sigma^*}{2\rho_g v_g^2}} \quad (19)$$

3.3. Model Prediction Results

To solve the model of VAD, we analyze the changes in jet diameter and wavelength under different operating conditions to compare their effects on the VAD. The trends are shown in Figure 4. The jet diameter decreases with increasing gas pressure and voltage, but as the gas pressure increases, the changes in jet diameter with voltage tend to become more moderate. The wavelength is mainly affected by gas pressure; when the gas pressure remains constant, the wavelength remains almost unchanged with increasing voltage. Under constant gas pressure, changes in jet diameter have a more significant effect on VAD, while under constant voltage, changes in wavelength have a more significant effect on VAD. It can also be observed that the high-voltage electric field has a noticeable refining effect on VAD.

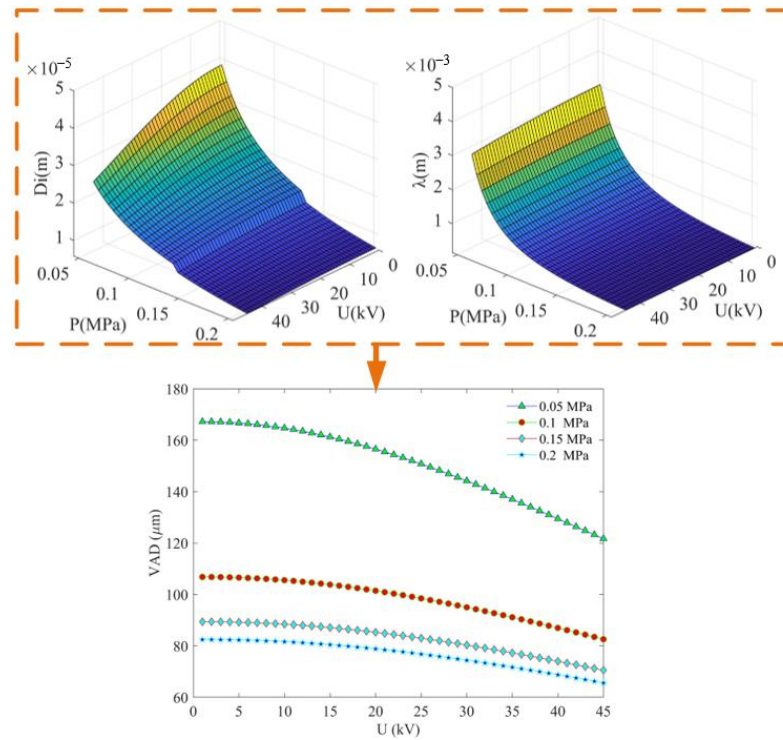


Figure 4. Variation trend of jet diameter, wavelength, and particle size under different working conditions.

3.4. Breakup of Small Liquid Droplets

In aerodynamic atomization, the study of droplet group atomization processes mainly focuses on the deformation and breakup of individual liquid droplets under the influence of external forces. Research indicates that the velocity difference between droplets and gas is the primary cause of small droplet breakup atomization. Surface tension promotes droplet shrinkage into spherical shapes, and viscous forces hinder droplet deformation. Only when external forces exceed internal forces will droplets undergo deformation or breakup. Typically, the Weber number is used to determine whether droplets will break up and the breakup morphology, which can be classified into five breakup modes: oscillatory breakup, bag breakup, multimodal breakup, shear breakup, and explosive breakup [38].

The Weber number represents the ratio of inertial force to surface tension effects. Its expression is

$$We = \frac{\rho_g v_r^2 D}{\sigma} \quad (20)$$

where v_r is the gas-liquid relative velocity (m/s). Based on the critical condition of droplet disturbance, the corresponding critical Weber number can be obtained:

$$We_r = \frac{8}{C_D} \quad (21)$$

After introducing an electrostatic field, the droplet surface carries a large amount of like charges, increasing its surface activity and reducing surface tension. Simultaneously, due to the action of the electric field force, the motion trajectory of the droplets is constrained. However, the influence of the electric field on droplet morphology is minimal, so the multistage breakup process of droplets under high-voltage electric fields can be analyzed through the droplet breakup mechanism in gas atomization. From the Weber number, it can be seen that the secondary breakup of droplets depends on the gas-liquid relative velocity and droplet surface tension, with surface tension decreasing as the charge increases.

4. Experimental Setup and Materials

4.1. Experimental Setup

To verify the model of VAD cone jet atomization, atomization performance experiments were carried out by measuring the experimental and theoretical values of droplet size under different gas pressures and voltages to compare and validate the accuracy of the model and evaluate atomization performance.

EMQL improves the problem of insufficient atomization performance and high aerosol concentration of traditional pneumatic atomization MQL, however, the parameterized controllable operation is more complicated due to the low integration of the equipment used in traditional EMQL. The innovative development of an integrated multi-energy field parametric control equipment, such as the multi-energy field driven electrostatic minimum quantity lubrication delivery device shown in Figure 5a, can realize the parametric control of air pressure, liquid flow, and voltage by designing the internal high-voltage electrostatic generation circuit, micro-pump control system, gas pressure control system, and human-machine operation interface. A controlled supply of air, liquid, and electricity to the nozzle shown in Figure 1 is achieved by this device.

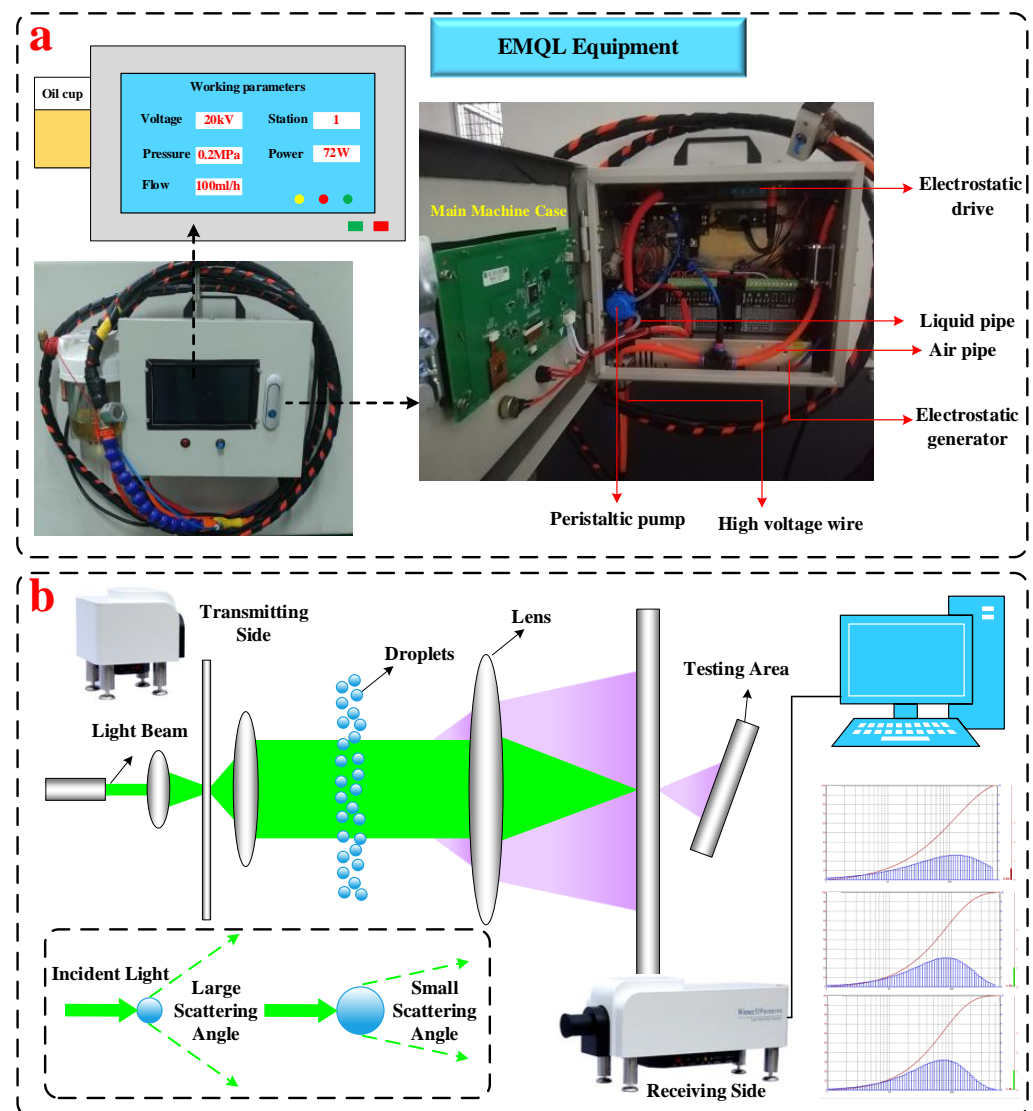


Figure 5. Experimental device for evaluating atomization performance. (a) schematic diagram of EMQL Equipment, (b) schematic diagram of VAD value acquisition.

The laser particle sizer (Winner319, Jinan Micro-nano Particle Instrument Co., Ltd., Jinan, China) is used to collect and measure the VAD of the droplets and their diameter distribution characteristics. Its working principle is shown in Figure 5b. The nozzle is placed vertically to spray droplets downward and the emitter emits a monochromatic parallel laser with the beam entering the droplet test area vertically below the nozzle. Droplets with different particle sizes cause the parallel beam to manifest a polydisperse Fraunhofer diffraction behavior. The diffraction angle produced by large-diameter droplets is small, whereas the diffraction angle produced by small-diameter droplets is large. Once the diffracted beam reaches the detector at the receiving end, the particle size distribution and the VADs of the droplets can be finally obtained using an energy spectral analysis apparatus. The laser particle sizer is used to obtain the R.S. value of the particle size distribution span and the percentage concentrations of PM₁₀ and PM_{2.5}. In consideration of the influence of the nozzle on the detection beam, the position 20 mm away from the nozzle outlet is selected as the atomization measurement point.

4.2. Experimental Materials

In industrial processing, the application of cutting fluid is a key factor affecting part formation and processing quality, and currently widely used mineral lubricating oils not only consume a lot but also cause serious pollution to the environment and workers' health. In contrast, biolubricants have good lubricating properties, such as a high flash point, low volatility, and high viscosity index. They are degradable and renewable green resources [39,40], and biolubricants, with their elongated fatty acid chains and polar groups, are more suitable for cutting and machining mechanical components [41]. With the introduction of microlubrication technology, biolubricants have been widely used in combination with MQL processes in the automotive manufacturing, aerospace, and rail transportation fields. Likewise, biolubricants are also well suited for EMQL technology. Soybean oil, as a relatively common vegetable oil, has moderate physical properties and is degradable, making it an ideal biolubricant [42]. Its physical properties are shown in Table 3.

Table 3. Physical property parameters of soybean oil at normal temperature [42].

Density (kg/m ³)	Surface Tension (N/m)	Relative Dielectric Constant	Power Viscosity (Pa·s)	Electrical Conductivity (mS/cm)
916.8	0.032	3.5	0.061	0.54

4.3. Experimental Scheme

Using a single-factor variable method, in each set of experiments, parameters such as liquid supply rate, and needle-plate electrode distance were kept constant, while the output voltage or gas pressure of the EMQL device was changed for comparative experiments. The role of the electric field was analyzed in terms of droplet size and distribution patterns. The applied voltage in the experiment was a negative high voltage, and the value only represented the magnitude of the voltage. The experimental scheme is shown in Table 4.

Table 4. Experimental scheme of atomization performance.

Atomization Parameters	Numerical Value
Liquid Flow (mL/h)	100
Gas Pressure (MPa)	0.05–0.4
Needle-plate Electrode Distance (mm)	50
Distance of Particle Size Measurement Position from Nozzle Outlet (mm)	20
Voltage Variation Range (kV)	0–40

5. Results

The modified electrostatic nozzle was used for atomization effect observation experiments. The actual measured values of VAD under various gas pressure conditions with voltage changes, as well as the comparison with the calculated volumetric average droplet size, is shown in Figure 6. When the gas pressure is higher than 0.2 MPa, the excessive gas pressure causes the microdroplets to move violently, exceeding the suppression range of the electrostatic field. The concentration of floating particles in the air increases, which seriously interferes with the experimental results. According to the exported data, the fluctuation of particle size values is so intense that it cannot be used as accurate reference data. Therefore, the experimental results under 0.05–0.15 MPa are given in the Figure. At 0.1 MPa, the particle size refinement is most apparent, with the particle size decreasing from 114.652 μm at 0 kV to 74.898 μm at 40 kV, a total reduction of 34.67%. This indicates that the average volumetric droplet size is significantly refined after lubricant-charged atomization.

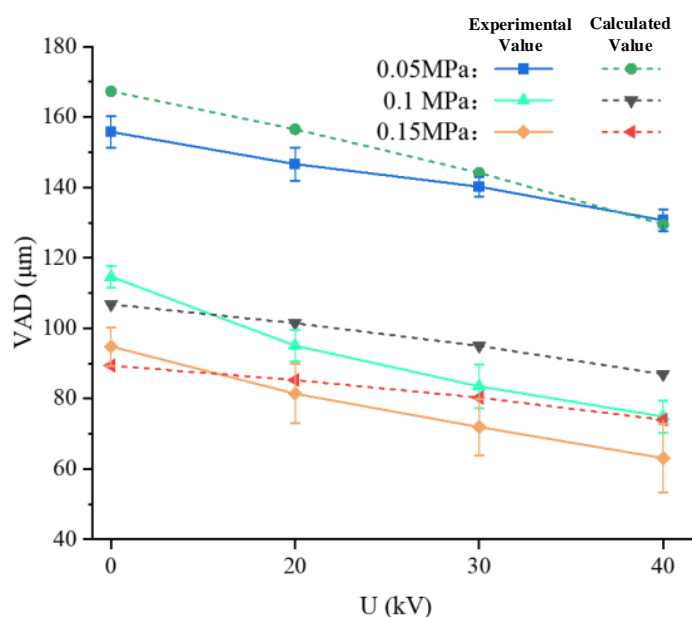


Figure 6. Comparison between theoretical and measured values of droplet size.

The experimental measurement of the volumetric average droplet size with changes in voltage and gas pressure is consistent with the theoretical calculation, showing an evident trend of decreasing particle size with increasing gas pressure and voltage. Under gas pressure conditions of 0.05–0.15 MPa, the errors of pure aerodynamic atomization are 6.9%, 7.4%, and 6.1%, respectively. When the voltage is within the 20–40 kV range at a gas pressure of 0.05 MPa, the error range is 0.93–6.3%. At 0.1 MPa gas pressure and a voltage within the 20–40 kV range, the error range is 6.3–12.1%. When the voltage is within the 20–40 kV range at a gas pressure of 0.15 MPa, the error range is 4.5–10.4%, with a rather random distribution of errors under various conditions.

In addition to the average volumetric droplet size, the atomization quality of the nozzle can be further revealed through the droplet group size distribution span value R.S. The smaller the R.S. value, the more uniform the droplet size and the higher the parameterization controllability. Its calculation formula is

$$R.S. = \frac{X_{90} - X_{10}}{X_{50}} \quad (22)$$

where X_{90} is the particle size with a cumulative distribution of 90%; X_{50} is the particle size with a cumulative distribution of 50%; and X_{10} is the particle size with a cumulative distribution of 10%.

The droplet group distribution span curve under various voltage conditions at 0.1 MPa gas pressure is shown in Figure 7. At 0 kV, the droplet size distribution is relatively wide, with an R.S. value of 3.934. After applying voltage, the R.S. value is the smallest at 40 kV, at 3.147, which is a 20% decrease compared to the R.S. value of pure aerodynamic atomization at 0.1 MPa.

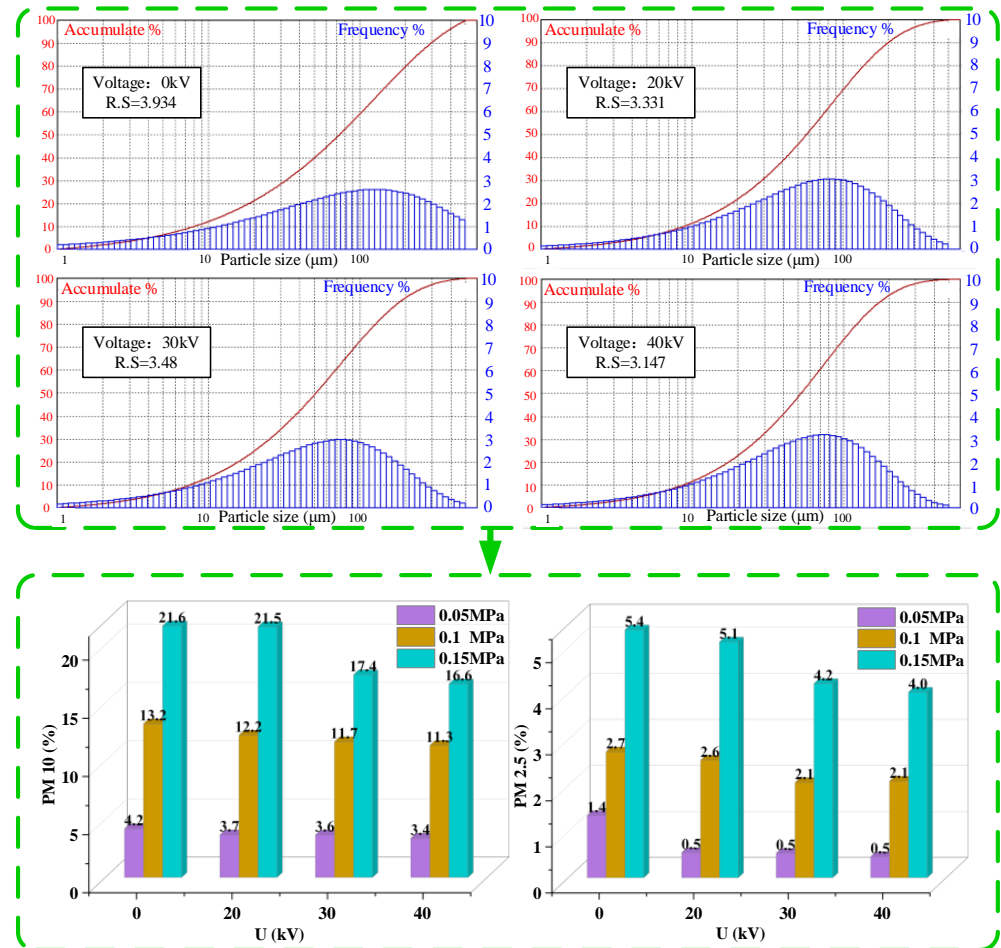


Figure 7. Microdroplet distribution law under different working conditions.

Considering the environmental damage and threats to the health of operators caused by the migration and dispersion of tiny oil mist particles during the atomization process, the PM_{2.5} and PM₁₀ percentage concentrations were also measured under different gas pressure and voltage conditions during the observation of droplet group distribution. As the gas pressure increases, the concentrations of PM_{2.5} and PM₁₀ significantly increase. It is believed that the increase in gas pressure leads to more intense energy exchange between the gas and liquid phases, increasing the probability of small liquid droplet breakage. During breakage, extremely small droplets are produced. The addition of an electric field has a noticeable inhibitory effect on the concentrations of PM_{2.5} and PM₁₀. As the voltage increases, the overall trend of PM_{2.5} and PM₁₀ concentrations decreases continuously. Under the three gas pressure conditions, the PM₁₀ percentage concentrations at 40 kV working conditions decreased by 19.05%, 14.39%, and 23.15% compared to pure aerodynamic atomization, respectively. At 40 kV working conditions, the PM_{2.5} percentage concentrations decreased by 64.29%, 22.22%, and 25.93% compared to the pure aerodynamic atomization working conditions, respectively.

6. Discussion

From the foregoing, it can be seen that the number of cone jets increases with increasing voltage, which is basically positively correlated, as shown in Figure 8. At a certain liquid flow rate, the higher the voltage applied to the nozzle, the finer and more uniform the diameter of the jet [33], and the more intense the fluctuations of the jet due to the intervention of the electric field, the denser the formation of wave crests, the probability of very large and very small particle size droplets is reduced. From the aforementioned electric field strength equation, it can be seen that as the voltage increases, the electric field strength near the needle electrode increases, and the droplet will be further broken, which leads to the formation of droplet size reduction and more concentrated distribution. It is worth noting that the standard deviation of droplet size decreases with increasing voltage at low air pressure, and the randomness of liquid atomization decreases and the controllability increases. As the energy exchange between gas and liquid phases increases, the randomness of liquid atomization increases significantly, leading to an increase in the fluctuation of experimental values.

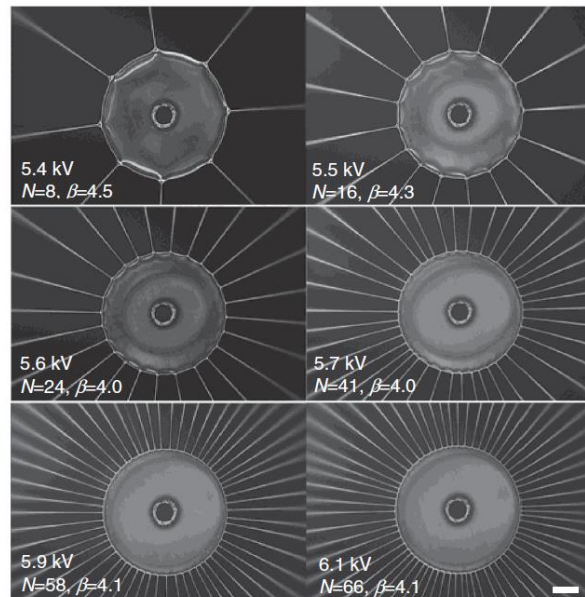


Figure 8. The number of jets versus voltage.

The liquid atomization is stretched by the external force to form multiple jets, and in the pure pneumatic atomization process, the unstable gas trajectory is likely to cause uneven distribution of liquid film and produce very fine liquid lines [31], as shown in Figure 9. The distribution of the liquid film is more uniform after charging, which reduces the probability of fine lines, and the surface tension of the liquid is reduced after adding the electric field, which reduces the retraction speed when the liquid line breaks and reduces the possibility of satellite droplets, thus effectively reducing the concentration of fine particles in the atomization process. Under the same voltage conditions, the concentration of $PM_{2.5}$ and PM_{10} increases significantly with the increase of air pressure, and the increase of air pressure will lead to a more intense energy exchange between the two phases of gas and liquid, the probability of breaking small liquid clusters increases, and the breaking will produce small droplets of very small particle size. In summary, the electrostatic field has a significant effect on particle size refinement, reducing the distribution width of droplet clusters and inhibiting the production of fine particles such as PM_{10} and $PM_{2.5}$.

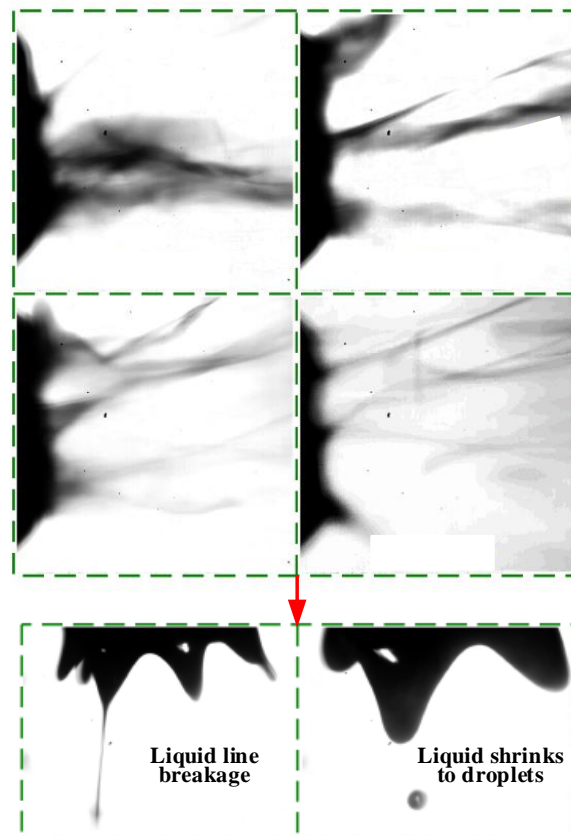


Figure 9. Morphological changes of the liquid line.

7. Conclusions

1. The charging process is mainly charge migration between the electrode and the lubricant and the droplet collision and adhesion with ions in the corona field, the charge of the lubricant depends on its own relative dielectric constant, the larger the dielectric constant the higher the charge, and the corresponding droplet surface tension is lower and easier to occur atomization;
2. The electrode cone jet atomization model was established. According to the model results, the volume average diameter of the droplet (VAD), the factors determining the VAD (jet diameter, wavelength) are negatively correlated with air pressure and voltage, and the jet diameter is more sensitive to voltage changes, while the wavelength is more sensitive to air pressure changes;
3. The VAD under different working conditions was measured by laser particle sizer, and the VAD refinement was most obvious at 0.1 Mpa, with an overall reduction of 34.67% and a 20% reduction in the droplet group size distribution span (R.S.). Moreover, the fine particulate matter percentage concentrations were significantly reduced under different air pressure conditions;
4. According to the comparison between the measured data and the results of the mathematical model, the theoretical and experimental values fit well, with an overall error of about 10%, which verifies the accuracy of the mathematical model.

Author Contributions: Data curation and writing—original draft preparation, H.M.; methodology, writing—review and editing, M.Y. All authors have read and agreed to the published version of the manuscript.

Funding: This research was funded by the National Natural Science Foundation of China (Grant No. 52205481), Shandong Natural Science Foundation (Grant No. ZR2020ME158), China Postdoctoral Science Foundation (2021M701810).

Data Availability Statement: The data presented in this study are available on request from the corresponding author. The data are not publicly available due to privacy or ethical restrictions.

Conflicts of Interest: The authors declare no conflict of interest.

References

1. Baldin, V.; Silva, L.R.R.d.; Davis, R.; Jackson, M.J.; Amorim, F.L.; Houck, C.F.; Machado, Á.R. Dry and MQL Milling of AISI 1045 Steel with Vegetable and Mineral-Based Fluids. *Lubricants* **2023**, *11*, 175. [[CrossRef](#)]
2. López de Lacalle, L.N.; Angulo, C.; Lamikiz, A.; Sánchez, J.A. Experimental and numerical investigation of the effect of spray cutting fluids in high speed milling. *J. Mater. Process Technol.* **2006**, *172*, 11–15. [[CrossRef](#)]
3. Özbek, O. Evaluation of Nano Fluids with Minimum Quantity Lubrication in Turning of Ni-Base Superalloy UDIMET 720. *Lubricants* **2023**, *11*, 159. [[CrossRef](#)]
4. Pereira, O.; Martín-Alfonso, J.E.; Rodríguez, A.; Calleja, A.; Fernández-Valdivielso, A.; López de Lacalle, L.N. Sustainability analysis of lubricant oils for minimum quantity lubrication based on their tribo-rheological performance. *J. Clean. Prod.* **2017**, *164*, 1419–1429. [[CrossRef](#)]
5. Liu, D.W.; Li, C.H.; Dong, L.; Qin, A.G.; Zhang, Y.B.; Yang, M.; Gao, T.; Wang, X.M.; Liu, M.Z.; Cui, X.; et al. Kinematics and improved surface roughness model in milling. *Int. J. Adv. Manuf. Technol.* **2022**. [[CrossRef](#)]
6. Shah, P.; Gadkari, A.; Sharma, A.D.; Shokrani, A.; Khanna, N. Comparison of machining performance under MQL and ultra-high voltage EMQL conditions based on tribological properties. *Tribol. Int.* **2021**, *153*, 106595–106601. [[CrossRef](#)]
7. Lv, T.; Xu, X.F.; Yu, A.; Hu, X. Oil mist concentration and machining characteristics of SiO₂ water-based nano-lubricants in electrostatic minimum quantity lubrication-EMQL milling. *J. Mater. Process Technol.* **2021**, *290*, 116964–116978. [[CrossRef](#)]
8. Su, Y.; Lu, Q.; Yu, T.; Liu, Z.; Zhang, C. Machining and environmental effects of electrostatic atomization lubrication in milling operation. *Int. J. Adv. Manuf. Technol.* **2019**, *104*, 2773–2782. [[CrossRef](#)]
9. Gupta, K.K.; Laubscher, R.F.; Davim, J.P.; Jain, N.K. Recent developments in sustainable manufacturing of gears: A review. *J. Clean Prod.* **2016**, *112*, 3320–3330. [[CrossRef](#)]
10. Jia, D.; Li, C.; Zhang, D.; Wang, S.; Hou, Y. Investigation into the Formation Mechanism and Distribution Characteristics of Suspended Microparticles in MQL Grinding. *Rec. Patents Mech. Eng.* **2014**, *7*, 52–62. [[CrossRef](#)]
11. Brentjes, A.; Jansen, B.; Pozarlik, A.K. Spray characteristics of an air-assisted electrostatic atomiser. *J. Elec.* **2022**, *115*, 103654–103661. [[CrossRef](#)]
12. Xu, W.; Li, C.; Zhang, Y.; Ali, H.M.; Sharma, S.; Li, R.; Yang, M.; Gao, T.; Liu, M.; Wang, X.; et al. Electrostatic atomization minimum quantity lubrication machining: From mechanism to application. *Int. J. Extrem. Manuf.* **2022**, *4*, 042003–042046. [[CrossRef](#)]
13. Huang, S.; Li, Z.; Yao, W.; Hu, J.; Xu, X. Tribological Performance of Charged Vegetable Lubricants. *Tribology* **2014**, *34*, 371–378. [[CrossRef](#)]
14. Huang, S.; Wang, Z.; Yao, W.; Xu, X.F. Tribological evaluation of contact-charged electrostatic spray lubrication as a new near-dry machining technique. *Tribol Int.* **2015**, *91*, 74–84. [[CrossRef](#)]
15. Quinchia, L.A.; Delgado, M.A.; Reddyhoff, T.; Gallegos, C.; Spikes, H.A. Tribological studies of potential vegetable oil-based lubricants containing environmentally friendly viscosity modifiers. *Tribol. Int.* **2014**, *69*, 110–117. [[CrossRef](#)]
16. Reddy, N.S.K.; Yang, M. Development of an electro static lubrication system for drilling of SCM 440 steel. *Proc. Inst. Mech. Eng. Part B J. Eng. Manuf.* **2010**, *224*, 217–224. [[CrossRef](#)]
17. Xu, X.F.; Huang, S.; Wang, M.; Yao, W. A study on process parameters in end milling of AISI-304 stainless steel under electrostatic minimum quantity lubrication conditions. *Int. J. Adv. Manuf. Technol.* **2017**, *90*, 979–989. [[CrossRef](#)]
18. Lin, J.; Lv, T.; Huang, S.; Hu, X.; Xu, X. Experimental Investigation on Grinding Performance Based on EMQL Technology. *CN Mech. Eng.* **2018**, *29*, 2783–2791+2798.
19. Huang, S.; Yao, W.; Hu, J.; Xu, X. Tribological Performance and Lubrication Mechanism of Contact-Charged Electrostatic Spray Lubrication Technique. *Tribol. Lett.* **2015**, *59*, 28–42. [[CrossRef](#)]
20. Huang, S.; Lv, T.; Wang, M.; Xu, X. Effects of Machining and Oil Mist Parameters on Electrostatic Minimum Quantity Lubrication-EMQL Turning Process. *Int. J. Precis. Eng. Man.* **2018**, *5*, 317–326. [[CrossRef](#)]
21. Huang, S.; Lv, T.; Wang, M.; Xu, X. Enhanced machining performance and lubrication mechanism of electrostatic minimum quantity lubrication-EMQL milling process. *Int. J. Adv. Manuf. Tech.* **2017**, *94*, 655–666. [[CrossRef](#)]
22. Jia, D.; Li, C.; Zhang, Y.; Yang, M.; Cao, H.; Liu, B.; Zhou, Z. Grinding Performance and Surface Morphology Evaluation of Titanium Alloy Using Electric Traction Bio Micro Lubricant. *J. Mech. Eng.* **2022**, *58*, 198–211. [[CrossRef](#)]
23. Jia, D.; Li, C.; Zhang, Y.; Zhang, D.; Zhang, X. Experimental research on the influence of the jet parameters of minimum quantity lubrication on the lubricating property of Ni-based alloy grinding. *Int. J. Adv. Manuf. Technol.* **2016**, *82*, 617–630. [[CrossRef](#)]
24. Jia, D.; Zhang, Y.; Li, C.; Yang, M.; Gao, T.; Said, Z.; Sharma, S. Lubrication-enhanced mechanisms of titanium alloy grinding using lecithin biolubricant. *Tribol. Int.* **2022**, *169*, 107461. [[CrossRef](#)]
25. Wang, X.; Deng, L.; Liu, Y.; Xie, P.; Yang, W. Taylor Cone Formation and Application. *Comput. Appl. Chem.* **2011**, *11*, 1387–1392.
26. Li, Q.; Tan, G.; Ji, X.; Yin, Y. Factors influencing the formation and fracture of Taylor cone. *J. Hebei Univ.* **2018**, *38*, 22–27.

27. Nie, Q.; Chen, H.; Li, S.; Gao, X.; An, Q.; Fang, H. Simulations for Pulsating Breakups of a Nano Taylor Cone. *J. Phys. Conf. Ser.* **2021**, *1995*, 012008–012014. [[CrossRef](#)]
28. Zhang, X.; Li, C.; Zhang, Y.; Yang, M.; Jia, D.; Hou, Y.; Zhang, N.; Li, R.; Ji, H. Experimental Study of Effect of Electric Field Parameters on Atomization Characteristics and Grinding Performance of Minimal Quantity Lubrication. *Manuf. Technol. Mach. Tool.* **2018**, *676*, 105–111. [[CrossRef](#)]
29. Liu, X.; He, W.; Yang, F.; Xiao, H.; Ma, J. Simulation and Analysis of Electron Transport Parameters in Air Discharge. *High Volt. Eng.* **2011**, *37*, 1614–1619. [[CrossRef](#)]
30. Jia, D.; Li, C.; Liu, J.; Zhang, Y.; Yang, M.; Gao, T.; Said, Z.; Sharma, S. Prediction model of volume average diameter and analysis of atomization characteristics in electrostatic atomization minimum quantity lubrication. *Friction* **2023**. [[CrossRef](#)]
31. TIAN, B.; YANG, D.; TANG, J.; LIU, Q. Some problems of the transmission/reflection method for measuring complex permittivity of materials. *CN J. Rad. Sci.* **2002**, *17*, 10–15.
32. Wang, L.; Dang, Z. Carbon Nanotube Filled Polymer-Based Dielectric Composites With High Dielectric Constant. *Trans. CN. Elect. Soc.* **2006**, *21*, 24–28.
33. Jiang, Y.; Ding, X.M.; Yu, S.P.; Gao, H.Y. Density-independent microwave measurement of material moisture content. *J. HIT* **2007**, *39*, 1829–1832.
34. Wang, Z.; Tian, Y.; Zhang, C.; Wang, Y.; Deng, W. Massively Multiplexed Electrohydrodynamic Tip Streaming from a Thin Disc. *Phys. Rev. Lett.* **2021**, *126*, 064502. [[CrossRef](#)] [[PubMed](#)]
35. Marmottant, P.; Villermaux, E. On spray formation. *J. Fluid Mech.* **2004**, *498*, 73–111. [[CrossRef](#)]
36. Varga, C.M.; Lasheras, J.C.; Hopfinger, E.J. Initial breakup of a small-diameter liquid jet by a high-speed gas stream. *J. Fluid Mech.* **2003**, *497*, 405–434. [[CrossRef](#)]
37. Bian, W.; Chen, X.; Wang, J. A critical comparison of two-fluid model, discrete particle method and direct numerical simulation for modeling dense gas-solid flow of rough spheres. *Chem. Eng. Sci.* **2019**, *210*, 115233. [[CrossRef](#)]
38. Pilch, M.; Erdman, C.A. Use of breakup time data and velocity history data to predict the maximum size of stable fragments for acceleration-induced breakup of a liquid drop. *Int. J. Multiph. Flow* **1987**, *13*, 741–757. [[CrossRef](#)]
39. Jia, D.Z.; Li, C.H.; Zhang, Y.B.; Yang, M.; Wang, Y.G. Current status and outlook of cooling lubrication for grinding process. *Mech. Eng. Auto.* **2017**, *202*, 201–202+205.
40. Singh, Y.; Sharma, A.; Singh, N.; Singla, A.; Rastogi, P.M. Prospects of inedible plant oil-driven bio-lubricants for tribological characteristics—A review. *Int. J. Ambient Energy* **2018**, *41*, 1534–1547. [[CrossRef](#)]
41. Alves, S.M.; Barros, B.S.; Trajano, M.F.; Ribeiro, K.S.B.; Moura, E. Tribological behavior of vegetable oil-based lubricants with nanoparticles of oxides in boundary lubrication conditions. *Tribol. Int.* **2013**, *65*, 28–36. [[CrossRef](#)]
42. Xie, Q.H.; Wu, S.X.; Liu, G.D.; Zhang, W.F. Application study of nano additives Al₂O₃ and MoS₂ in oil-in-water drop jet cooling. *Tool Eng.* **2023**, *57*, 39–45.

Disclaimer/Publisher’s Note: The statements, opinions and data contained in all publications are solely those of the individual author(s) and contributor(s) and not of MDPI and/or the editor(s). MDPI and/or the editor(s) disclaim responsibility for any injury to people or property resulting from any ideas, methods, instructions or products referred to in the content.